

# Chapter 4

## Group-velocity tomography at Valhall

In this chapter I show that Love and Scholte wave group velocity images, retrieved by crosscorrelating microseism noise, provide complimentary information about the subsurface. Love wave group velocities carry a strong imprint of production-induced subsidence-related stresses in the overburden. Scholte group velocities image paleochannels and other geology known to exist in the top 300 m of the subsurface. The regularization strength is normalized for all inversions of traveltime picks from crosscorrelations of a particular stack length (stacking crosscorrelations for 6 hours, 12 hours, or 24 hours of noise recordings). This allows for one-on-one comparisons between images. Quantification of the expected variance between tomography images from consecutively recorded periods providing a temporal resolution.

### INTRODUCTION

After the initial successes of seismic interferometry from ambient noise (Campillo and Paul, 2003; Shapiro and Campillo, 2004), surface waves retrieved by noise correlations became a popular source for tomography studies (Sabra et al., 2005b; Shapiro et al., 2005; Yao et al., 2006; Gerstoft et al., 2006). The widespread application and

success of seismic interferometry at regional and crustal scales spurred interest in exploration-scale applications. A preliminary study of an ocean-bottom-node (OBN) recording over the Astero field in the northern North Sea yielded images of group velocities between 0.18 Hz and 0.4 Hz that correlate with known structures (Bussat and Kugler, 2011). Previous studies of ambient seismic noise group-velocity tomography at Valhall only utilized Scholte waves and produced images for a few central frequency ranges, but they successfully imaged paleochannels a few hundred meters deep in the subsurface (de Ridder, 2011; de Ridder and Dellinger, 2011; de Ridder, 2012; de Ridder and Biondi, 2013; Mordret et al., 2013a). These buried paleochannels were previously known to exist based on P-wave full waveform inversion (Sirgue et al., 2010). De Ridder and Biondi (2013) found the noise tomography to be stable and repeatable.

As seen in Chapter 3, the crosscorrelations of vertical-to-vertical component geophones (recording particle velocities) reveal Estimated Green's functions (EGFs) dominated by fundamental-mode Scholte waves. Crosscorrelations of transverse-to-transverse components (with respect to the station couple back azimuth) of particle velocities reveal EGFs dominated by fundamental mode Love waves. This mode separation is used in this chapter to create images of Scholte- and Love-wave group velocities with high repeatability using as little as 6 hours. The wavelengths for fundamental-mode Scholte waves range from over 550 m for the lowest central frequency range to 390 m (Chapter 3). Longer wavelengths provide sensitivity to medium parameters further from the interface of propagation (e.g., deeper regions of the earth). Because the properties of the earth vary with depth, the surface waves are dispersive, and different frequencies offer us information about different depth levels (Aki and Richards, 2002).

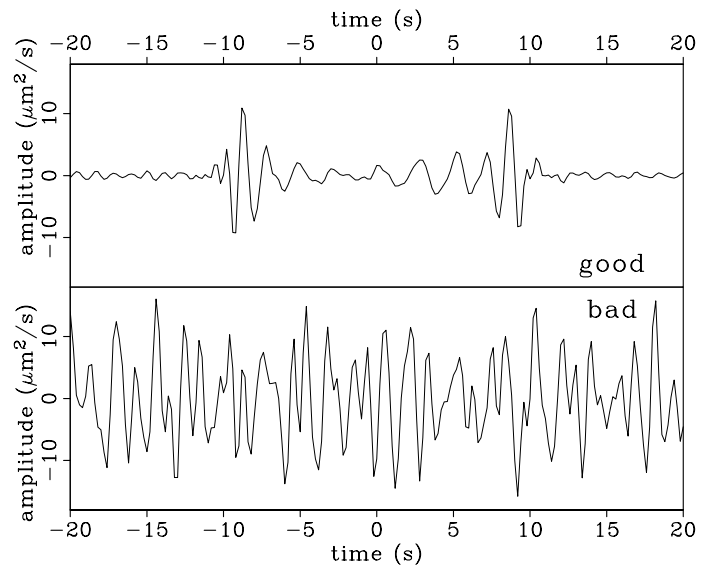
The chapter begins with an introduction to straight-ray tomography inversion. Then group velocity images are presented for Love and Scholte waves at central frequency regimes ranging from 0.55 Hz to 1.55 Hz. The tomography results are proven stable by testing various crosscorrelation stack lengths for three data sets collected in 2004, 2005 and 2010.

## STRAIGHT-RAY TOMOGRAPHY FOR GROUP-VELOCITY IMAGES

True group velocities are approximated by apparent group-velocity images because the observed phase velocities and group velocities are modified by scattering and bending of surface waves in three dimensions (Wielandt, 1993) (Chapter 1). Different frequencies provide information about different depth levels (Aki and Richards, 2002). Apparent group velocities of the interface waves can be found for packages of energy isolated within a narrow frequency range (Claerbout, 1976). The aim is to create Scholte-wave group-velocity images at different frequencies (as a proxy for depth) by picking a group traveltime as the peak of the envelope after a narrow-range bandpass. An initial screening of the crosscorrelations identified a set of stations with poor quality or fainter crosscorrelation signals (Figure 4.1), those stations were discarded. Figure 4.2a shows crosscorrelation results for the data recorded by the geophones belonging to the same cable with the data recorded by the first geophone on the left. The wave-train propagating outward is dispersive, the zero crossings moving faster than the wave train as a whole. Traveltime picking was performed once for each station pair and the reciprocal crosscorrelation was discarded.

Figure 4.1: Example of a good (top) and bad (bottom) crosscorrelation signal. [CR]

goodandbad



## Preprocessing

The purpose of the preprocessing is to make the traveltimes insensitive to variations in the amplitude spectrum of the ambient seismic field. The bandpass filter is implemented in the frequency domain by a taper. The taper is constructed with a flat response over a 0.2 Hz interval (the center frequency range) and Hann-tapers over an additional 0.2 Hz on both sides. To balance the spectra of the EGFs, the original amplitude is discarded and replaced by the taper. The Fourier domain analytic signal is constructed by multiplying the complex trace with the heaviside function. After inverse Fourier transformation, the traveltimes are picked as the envelope peak. A signal-to-noise ratio (SNR) is defined as the ratio between the maximum of the envelope within an estimated linear moveout window (5 s wide) to the average of the envelope outside the moveout window. Strong residual energy outside of the moveout window would decrease the SNR. The moveout window was visually determined by graphically inspecting the result (Figure 4.2). This procedure is used for a traveltimes pick from causal and anticausal portions of the EGFs and for a traveltimes pick after symmetrizing the EGFs. An indicator of poor EGF retrieval is the difference between causal and anticausal parts. However, neither the absence or presence of differences between causal and anticausal parts can be a conclusive indicator of quality (Chapter 1). Given  $N$  stations in an array, this leads to  $N(N - 1)/2$  interstation traveltimes picks. This traveltimes picking sequence is summarized in Algorithm 1.

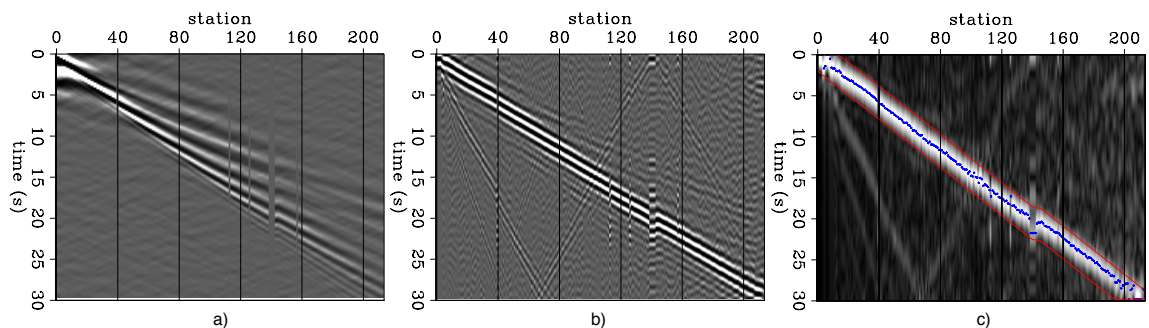


Figure 4.2: a) crosscorrelation gather, b) bandpassed, spectrally balanced crosscorrelation gather, c) picked envelope function of the bandpass-filtered spectrally balanced crosscorrelation gather in (a). [CR] `traveltimespick`

---

**Algorithm 1** Traveltime picking
 

---

```

for is=1,ns do
  for ir=is+1,nr do

    trace = fft{data(ir, is)}

    phase = atan2{imag{trace}, real{trace}}
    trace = taper · cexp{0, phase}

    trace = real{ifft{trace}}

     $t^+$  ← maxloc{mask · trace}
    trace = reverse{trace}
     $t^-$  ← maxloc{mask · trace}
    trace = reverse{trace} + trace
     $t$  ← maxloc{mask · trace}

    weight = sum{ $H \cdot (1 - \text{mask}) \cdot \text{trace}$ } · sum{ $H \cdot (1 - \text{mask})$ }-1
     $SNR$  = weight · maxval{mask · trace}

  end for
end for

```

---

*Taper* is the frequency-domain Hann taper for bandpassing with non-zero weights for positive frequencies only, *mask* is the time-domain masker that selects moveout window for positive times only, and  $H$  denotes the heaviside function. Array indices are omitted when obsolete for the statement and  $\{\cdot\}$  denotes an explicit element by element multiplication. The algorithm combines the computation of the analytic signal and spectral whitening. The inputs are the time-domain crosscorrelation signals, *data*. The computed traveltime picks for the causal, anticausal and symmetrized crosscorrelation signals, respectively  $t^+$ ,  $t^-$  and  $t$ , and signal to noise ratio,  $SNR$ , are collected and become the output of the algorithm.

---

A subset of the traveltimes picks form the input to a tomographic inversion of the group-wave velocity map that predicts the observed traveltimes. The following selection criteria were applied:

- A minimum and maximum interstation offset ( $\Delta x$ ).
- A maximum velocity equivalence for the traveltimes pick difference between the causal and anticausal portions of the EGFs ( $\frac{|t^+ - t^-|}{\Delta x}$ ).
- A minimum signal to noise ratio.

These criteria aim to discard the worst traveltimes picks yet keep nearly a million picks for the inversion. To directly compare tomographic images based on crosscorrelations of equal stack length there is an additional criterion:

- The total number of kept traveltimes picks (based on best SNR ratio).

These selection criteria will be further specified in later sections.

## Straight-ray tomography formulation

For each tomography problem,  $N$  traveltimes from the symmetrized EGFs were selected,  $\mathbf{t} = (t_1, t_2, \dots, t_N)^T$ , using the procedure described above. These traveltimes are predicted from a slowness model space,  $\mathbf{m}$ , and by a straight-ray tomography operator,  $\mathbf{F}$ . The problem is posed as a perturbation,  $\Delta\mathbf{m}$ , of an average slowness. The average slowness,  $m_0$ , is computed from the traveltimes picks:

$$m_0 = \frac{1}{N} \sum_{i=1}^N \frac{t_i}{\Delta x_i}. \quad (4.1)$$

The contribution of the average slowness is subtracted from the traveltimes picks, yielding traveltimes residuals  $\Delta\mathbf{t} = (\Delta t_1, \Delta t_2, \dots, \Delta t_N)^T$ :

$$\Delta\mathbf{t} = \mathbf{t} - m_0 \Delta\mathbf{x}, \quad (4.2)$$

where  $\Delta \mathbf{x} = (\Delta x_1, \Delta x_2, \dots, \Delta x_N)^T$  is a vector that contains the offsets,  $\Delta x$ , for each specific traveltimes pick. The remaining traveltimes residuals are predicted from a perturbation slowness model,  $\Delta \mathbf{m}$ , by a straight-ray tomography operator,  $\mathbf{F}$ :

$$\Delta \mathbf{t} = \mathbf{F} \Delta \mathbf{m}. \quad (4.3)$$

This operator,  $\mathbf{F}$ , is a slowness integration kernel where each row contains the distances through each model cell of a straight line connecting a specific source-receiver couple (Figure 4.3). A conjugate-direction algorithm is used to find the minimum of the following  $L^2$  norm:

$$\left\| \mathbf{F} \Delta \mathbf{m} - \Delta \mathbf{t} \right\|_2^2 + \epsilon \left\| \nabla^2 \Delta \mathbf{m} \right\|_2^2, \quad (4.4)$$

where the Laplace operator,  $\nabla^2$ , is used as regularization to force a smooth model. The inversion problem is first solved with a very large regularization strength (epsilon)  $\epsilon = 1 \times 10^{10}$ . The traveltimes picks corresponding to the largest 2.5 percentile misfits are discarded and the inverse problem is solved again. This approach is an approximation to optimization by reweighted least squares. After inversion, the slowness models can be recovered from the perturbation map by adding the average slowness,  $\mathbf{m} = \Delta \mathbf{m} + m_0$ . A velocity image is derived as the inverse of the slowness model. The model space is formed by 90 east-west and 110 north-south grid cells, each 100 m by 100 m wide. The grid cell size is smaller than the resolution of the wavelength, so the regularization plays an important role in finding reasonable solutions. The regularization will widen the sensitivity of the ray, thus partially accounting for finite-frequency effects and ray bending (Ritzwoller et al., 2002). Furthermore, in a dense network such as a LoFS array, the tomography is very sensitive to differences in station couples with large overlapping ray sections, effectively providing sensitivity to the gradient of the wavefront.

Figure 4.4 shows inverted Scholte wave group-velocity images that were obtained for regularization strengths ranging from  $\epsilon = 0$  to  $\epsilon = 2.94 \times 10^8$  and for central frequency ranges 0.75 – 0.95 Hz (4.4a to j) and 1.35 – 1.55 Hz (4.4k to t). Traveltimes

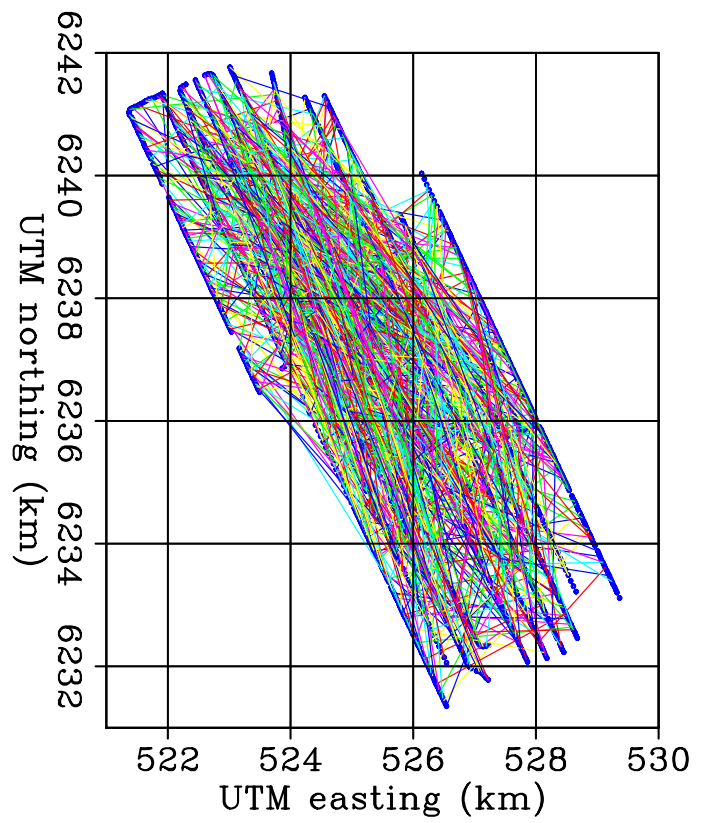


Figure 4.3: Example of straight-ray paths and coverage, showing only 0.1% of all rays used for a typical inversion. [CR] rays

were picked on the stack of all 2010 data of vertical to vertical crosscorrelations. The minimum and maximum offsets for traveltime picks selected were 1500 m and 6000 m; these bounds were based on a visual inspection as in Figure 4.2. The maximum velocity-equivalent of the anti-symmetry in traveltimes (picked on correlation signals before symmetrizing) was 345 m/s for 0.75 – 0.95 Hz and 315 m/s for 1.35 – 1.55 Hz. Only the best 900,000 traveltimes (based on best SNR ratios) for 0.75 – 0.95 Hz and the best 1,000,000 traveltime picks for 1.35 – 1.55 Hz were kept. The effect of increasing epsilon is substantial when epsilon is relatively small (compare Figure 4.4a to Figure 4.4b and Figure 4.4k to Figure 4.4l), but the effect of increasing epsilon diminishes for larger values of epsilon (Figure 4.4). Generally, an optimum epsilon can be chosen through an L-curve analysis (Aster et al., 2005), which requires plotting data and model objective fitting residuals. This analysis is included later in this chapter. However, from Figure 4.4 it is already apparent that the regularization strength suppresses elongated anomalies (streaks) that lie between the receiver lines. The resolution analysis at the end of the next section analyses the residual as a function of regularization strength projected into the model space.

## SCHOLTE- AND LOVE-WAVE GROUP-VELOCITY IMAGES

The vertical-to-vertical component crosscorrelations are dominated by fundamental-mode Scholte waves and the transverse-to-transverse component crosscorrelations are dominated by fundamental-mode Love waves (Chapter 3). Picking traveltimes in EGFs from vertical-to-vertical component crosscorrelations yields traveltimes for Scholte waves, while picking the transverse-to-transverse crosscorrelations yields traveltimes for Love waves. Traveltimes are picked for nine different central frequency ranges. The moveout velocity was determined using a visual analysis (Figure 4.2) that also yielded an offset range for which nearby picks appeared consistent for nine different central frequency ranges. The determined offset range and the maximum acceptable anti-symmetry for nine different central frequency ranges are summarized

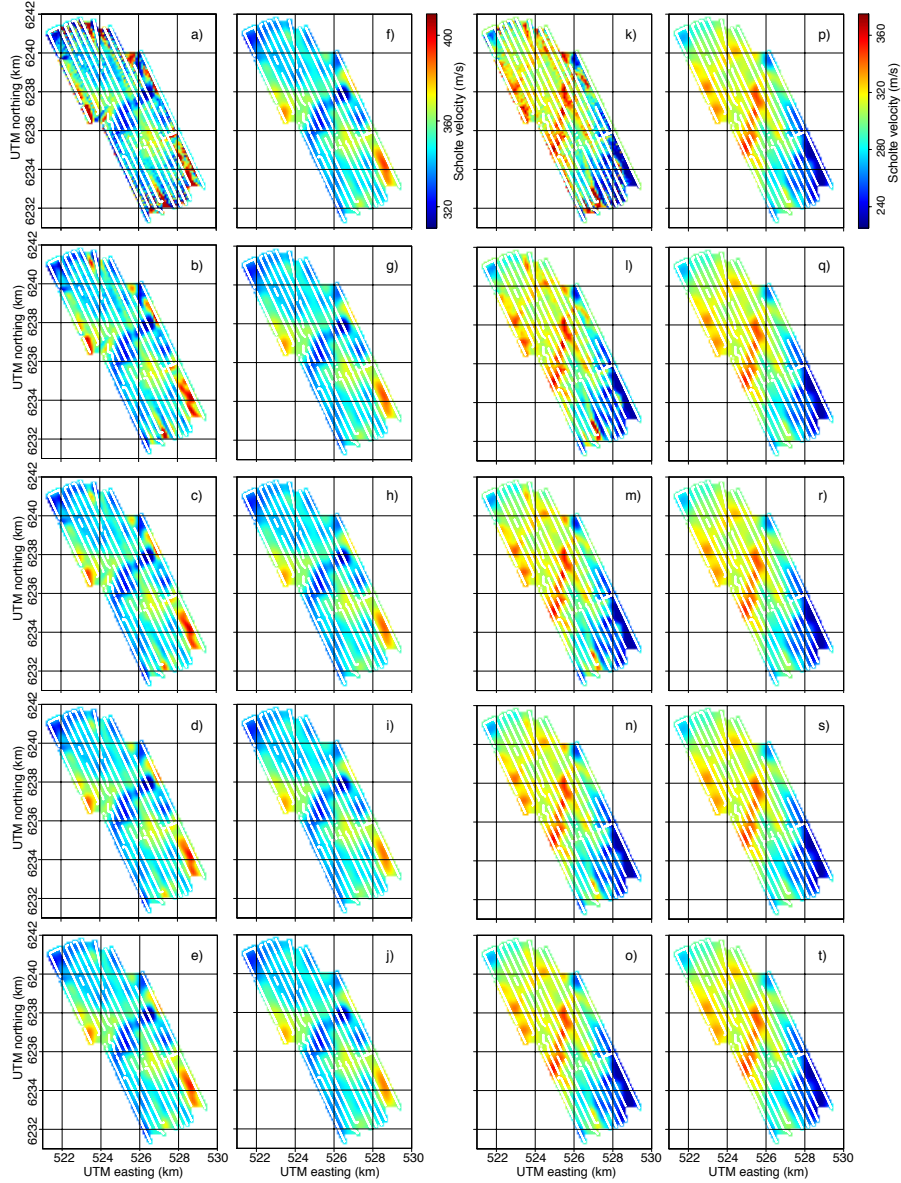


Figure 4.4: Scholte-wave group-velocity images as a function of regularization strength ( $\epsilon$ ) from the stack of all crosscorrelations of 2010 data. Left two columns, a) to j), group-velocity for 0.75 – 0.95 Hz, right two columns, k) to t), group-velocity for 1.35 – 1.55 Hz. Regularization: in a) and k)  $\epsilon = 0$ , in b) and l)  $\epsilon = 2.4 \times 10^7$ , in c) and m)  $\epsilon = 5.4 \times 10^7$ , in d) and n)  $\epsilon = 8.4 \times 10^7$ , in e) and o)  $\epsilon = 11.4 \times 10^7$ , in f) and p)  $\epsilon = 14.4 \times 10^7$ , in g) and q)  $\epsilon = 17.4 \times 10^7$ , in h) and r)  $\epsilon = 20.4 \times 10^7$ , in i) and s)  $\epsilon = 23.4 \times 10^7$ , in j) and t)  $\epsilon = 26.4 \times 10^7$ . [CR] joseph-all-vs-eps-C3-C6

Center frequency range (Hz)	$\{\Delta x\}_{\min}$	$\{\Delta x\}_{\max}$	$\left\{\frac{ t^+ - t^- }{\Delta x}\right\}_{\max}$	Number of traveltimes picks	Average group velocity (m/s)
0.55 – 0.75 Hz	1500	6000	0.0000500	944083	363.7
0.65 – 0.85 Hz	1500	6000	0.0000750	1169851	355.4
1.75 – 0.95 Hz	1500	6000	0.0001000	1188926	348.0
1.85 – 1.05 Hz	1500	6000	0.0001250	1194287	341.1
0.95 – 1.15 Hz	1500	6000	0.0001500	1190935	333.0
1.05 – 1.25 Hz	1500	6000	0.0001750	1182368	323.9
1.15 – 1.35 Hz	1500	6000	0.0002000	1171199	316.1
1.25 – 1.45 Hz	1500	5000	0.0002250	986402	308.8
1.35 – 1.55 Hz	1500	5000	0.0002500	954262	303.3

Table 4.1: Traveltime picking and acceptance criteria in EGFs from vertical-to-vertical component crosscorrelations.

Center frequency range (Hz)	$\{\Delta x\}_{\min}$	$\{\Delta x\}_{\max}$	$\left\{\frac{ t^+ - t^- }{\Delta x}\right\}_{\max}$	Number of traveltimes picks	Average group velocity (m/s)
0.55 – 0.75 Hz	1500	3500	0.0000500	161437	395.0
0.65 – 0.85 Hz	1500	4000	0.0000750	314213	385.5
1.75 – 0.95 Hz	1500	5000	0.0001000	575768	378.7
1.85 – 1.05 Hz	1500	6000	0.0001250	832868	370.3
0.95 – 1.15 Hz	1500	6000	0.0001500	884395	360.5
1.05 – 1.25 Hz	1500	5000	0.0001750	748452	347.8
1.15 – 1.35 Hz	1500	4000	0.0002000	559763	333.1
1.25 – 1.45 Hz	1500	4000	0.0002250	558613	325.0
1.35 – 1.55 Hz	1500	3500	0.0002500	427133	316.8

Table 4.2: Traveltime picking and acceptance criteria in EGFs from transverse-to-transverse component crosscorrelations.

in Tables 4.1 and 4.2 for Scholte wave and Love wave traveltimes, respectively.

The resulting traveltimes are now input to the straight-ray tomography procedure to yield Scholte-wave group-velocity and Love-wave group-velocity images (Figures 4.5 and 4.6, respectively). The regularization strength used for these inversions was  $\epsilon = 1.14 \times 10^8$ . Tables 4.1 and 4.2 list for each central frequency range, the number of selected picks (after discarding the largest 2.5 percentile of misfits in a strongly regularized inversion) and their corresponding average velocities,  $m_0^{-1}$ , for Scholte and Love waves, respectively.

The Scholte-wave velocity images in Figure 4.5 show several features that are dominant in different central frequency regimes. These features are annotated with capital letters in Figure 4.7a and 4.7b. A low-velocity anomaly crosses the center of the array from southwest to northeast just south of the main platform at central

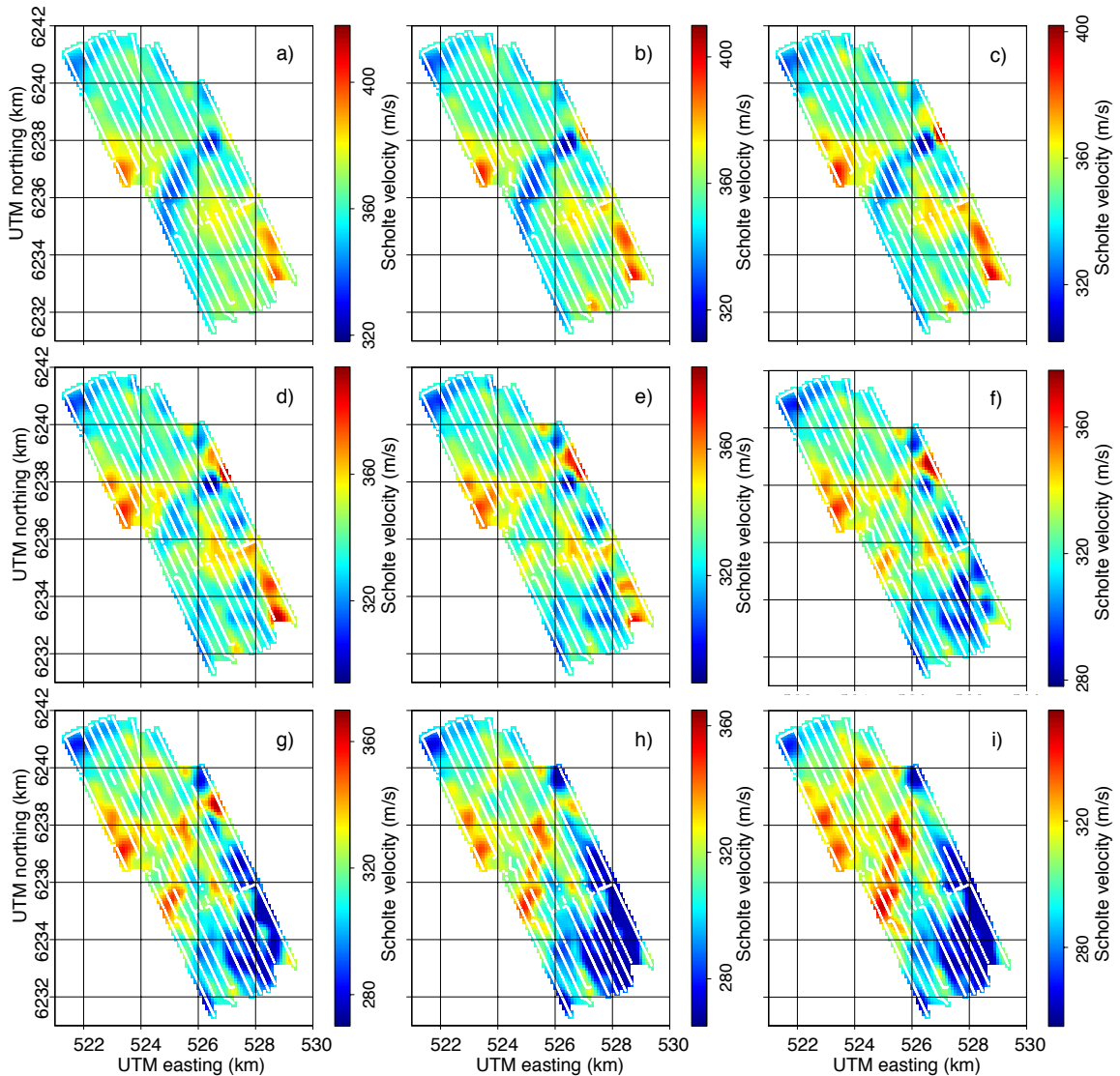


Figure 4.5: Scholte-wave group-velocity images from the stack of all crosscorrelations of 2010 data. Group-velocity for: a) 0.55–0.75 Hz, b) 0.65–0.85 Hz, c) 0.75–0.95 Hz, d) 0.85–1.05 Hz, e) 0.95–1.15 Hz, f) 1.05–1.25 Hz, g) 1.15–1.35 Hz, h) 1.25–1.45 Hz, i) 1.35–1.55 Hz. [CR] `valhall-v-tomos`

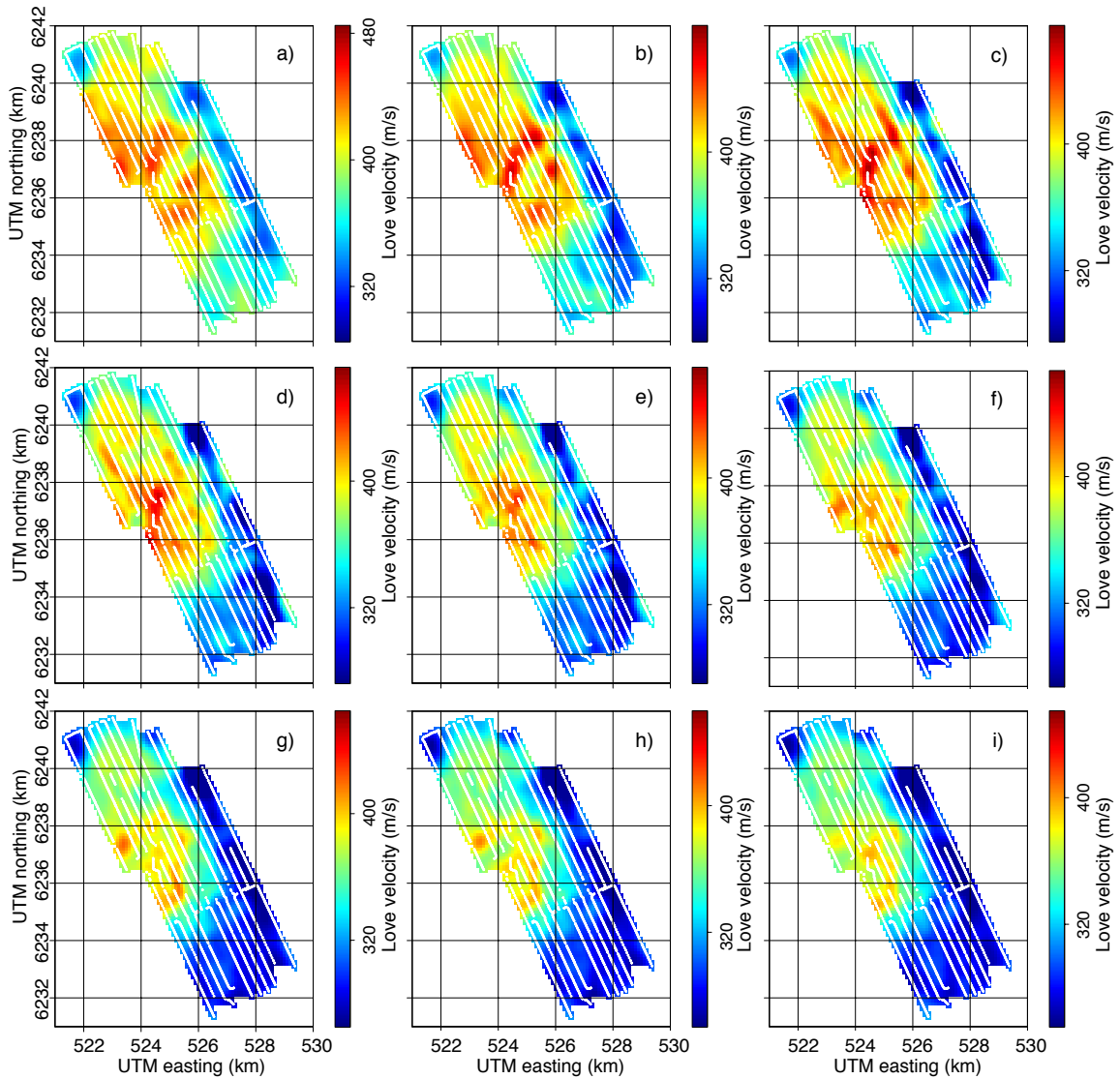


Figure 4.6: Love-wave group-velocity images from the stack of all crosscorrelations of 2010 data. Group-velocity for: a) 0.55–0.75 Hz, b) 0.65–0.85 Hz, c) 0.75–0.95 Hz, d) 0.85–1.05 Hz, e) 0.95–1.15 Hz, f) 1.05–1.25 Hz, g) 1.15–1.35 Hz, h) 1.25–1.45 Hz, i) 1.35–1.55 Hz. [CR] `valhall-t-tomos`

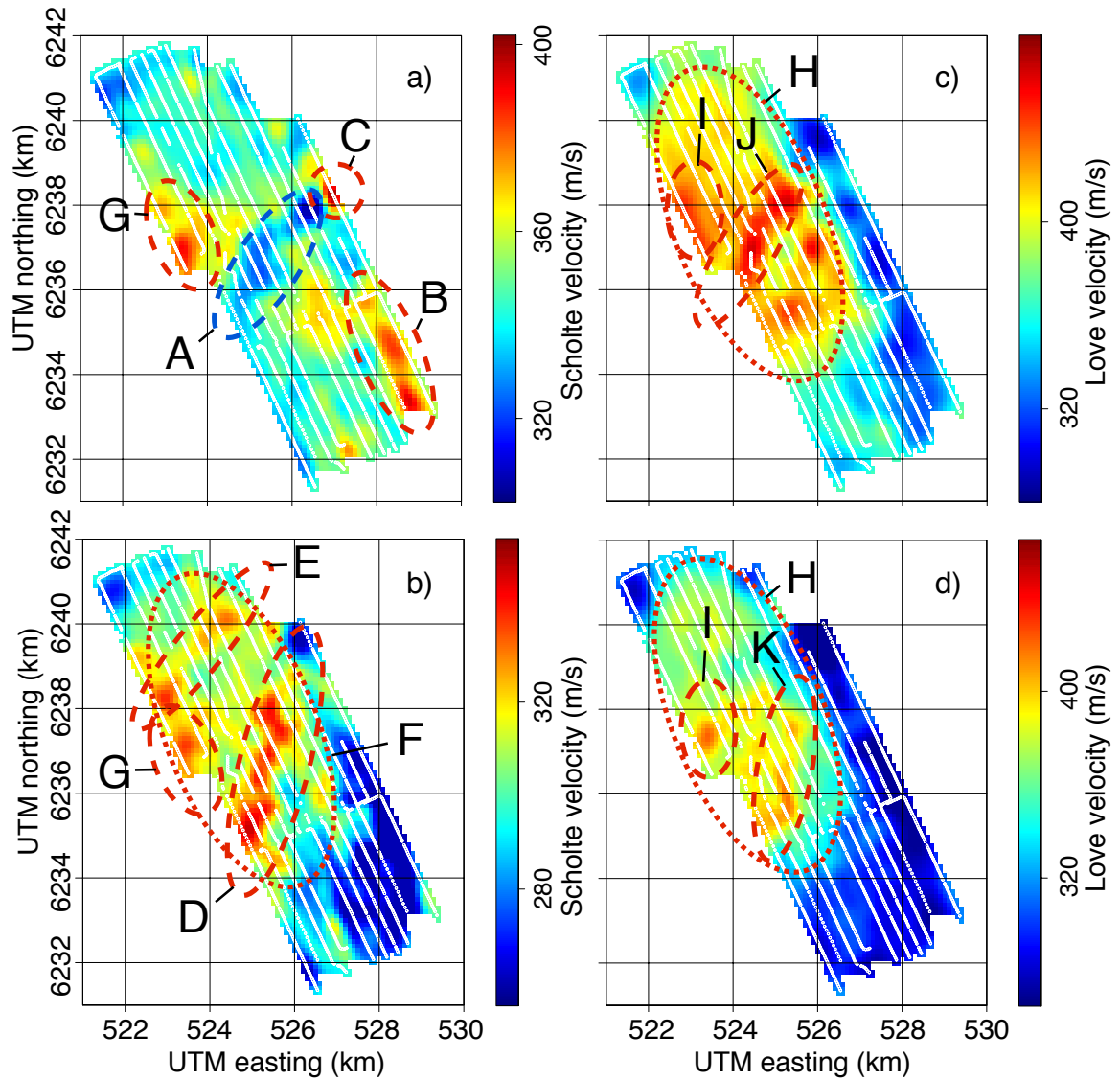


Figure 4.7: Annotated Love- and Scholte-wave group-velocity images. Scholte-wave group-velocity images for: a) 0.75 – 0.95 Hz, b) 1.35 – 1.55 Hz. Scholte-wave group-velocity images for: c) 0.65 – 0.85 Hz, d) 1.15 – 1.35 Hz. [CR]

joseph-tomo-C3-C6-ann

frequency ranges 0.55–1.15 Hz (A). Furthermore, a high-velocity anomaly is observed in the southeast corner of the array (B). A small high-velocity anomaly appears up two thirds along the eastern edge of the array at central frequency ranges 0.65 – 1.35 Hz (C). A meandering channel crosses the array from south-southwest to north-northwest at central frequency ranges 1.15 – 1.55 Hz (D). An anomaly that crosses the northern half of the array in the southwest to northeast direction is best observed at central frequency ranges 1.35 – 1.55 Hz (E). A large oval-shaped background higher velocity zone is located in the northern part of the array (F). Finally, one or more high-velocity anomalies are imaged just west-northwest of the main platforms for the entire frequency regime (G).

The Love-wave velocity images in Figure 4.6 also show several features that are dominant in different central frequency regimes. These features are annotated with capital letters in Figures 4.7c and 4.7d. The most dominant feature in all central frequency regimes is a large oval-shaped zone of higher background velocity in the northern part of the array (H). One or more high velocity anomalies are imaged just west of the platform at all central frequency ranges (I). A high-velocity anomaly is seen directly under the platforms at central frequency ranges 0.55 – 1.15 Hz (J). A meandering anomaly is imaged just east-southeast of the platforms at a central frequency regime of 1.15 – 1.55 Hz (K). Unlike the anomalies in the Scholte wave velocity images (Figure 4.5), this meandering anomaly does not cross the entire array.

Given the uncertainty in the data, in the absence of model priors, the spatial resolution of the inversion is given by the covariance between the posterior likelihoods on adjacent model parameters. However, uncertainty of the traveltimes picks is inherently very hard to estimate using the picking procedures described previously. The width of the envelope function is determined by the bandwidth of the central frequency range. The spectral amplitudes do not carry information because they were balanced before envelope computation. However, the inconsistency of picks in adjacent traces, given reasonable velocities, provide information about the noise. The information on the noise is implicitly included in the inversion by posing the problem as over-determined. The regularization is responsible for enforcing a geologically reasonable model. With

increasing regularization strength, the covariance between the posterior likelihoods on adjacent model parameters also increases, and the resolution provided by the energy of the data-fitting objective goes down. The regularization strength must be chosen such that it does not smooth geologically reasonable anomalies (Figure 4.4).

Three measures of resolution for the Scholte wave group-velocity tomography between 0.75 – 0.95 Hz (Figure 4.5c) are shown in Figure 4.8 and 4.9. The first measure of resolution is the ray-coverage, which is quantified by the cumulative ray-length through each model cell (Figure 4.8a). The center of the array is very well covered, while the edges are less well covered. The second measure is a checkerboard test. The checkerboard test provides an intuitive measure of resolution by recovering the checkerboard grid pattern shown in Figure 4.8b given the ray path coverage and the regularization strength. The difference between causal and anticausal traveltimes was added as a proxy for the noise in the data (although its effect was negligible unless increased by two orders of magnitude). The edges of the recovered checkerboard grid cells are significantly smoothed by the regularization (Figure 4.8c). The checkerboard grid cells are not always resolved well at the edges of the array due to biased azimuthal coverage of the traveltimes picks. I studied results of applying the adjoint of the tomographic operator applied to the final data misfit (Figure 4.9) to detect if there is energy in the misfit that should be in the model. This confirms the choice for regularization strength because the misfit is dominated by streaks interpreted to be acquisition imprint. The only exception is some energy related to the very high velocity contrast at the border between low-velocity anomaly A and high-velocity anomaly C (Figure 4.7), indicated with an arrow in Figure 4.9d.

## REPEATED SCHOLTE-WAVE AMBIENT-NOISE TOMOGRAPHY

It is interesting to explore whether the retrieval of the Scholte-wave velocity images shown in the previous section can be performed using shorter recordings. Stacking a certain amount of crosscorrelations results in EGFs with a different background

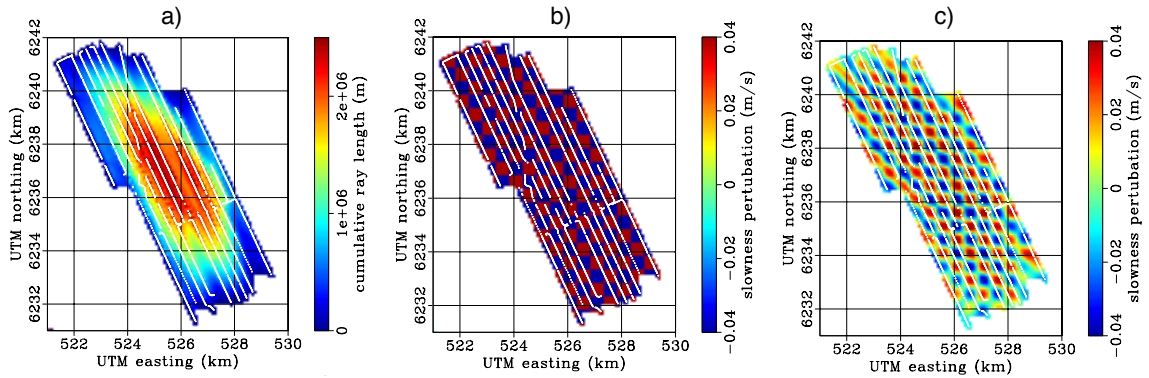


Figure 4.8: Resolution indicators for Scholte-wave images. a) cumulative ray-length through each cell for the Scholte wave group velocity tomography between 0.75 – 0.95 Hz, b) model checkerboard grid, c) retrieved checkerboard grid. [CR] resolution

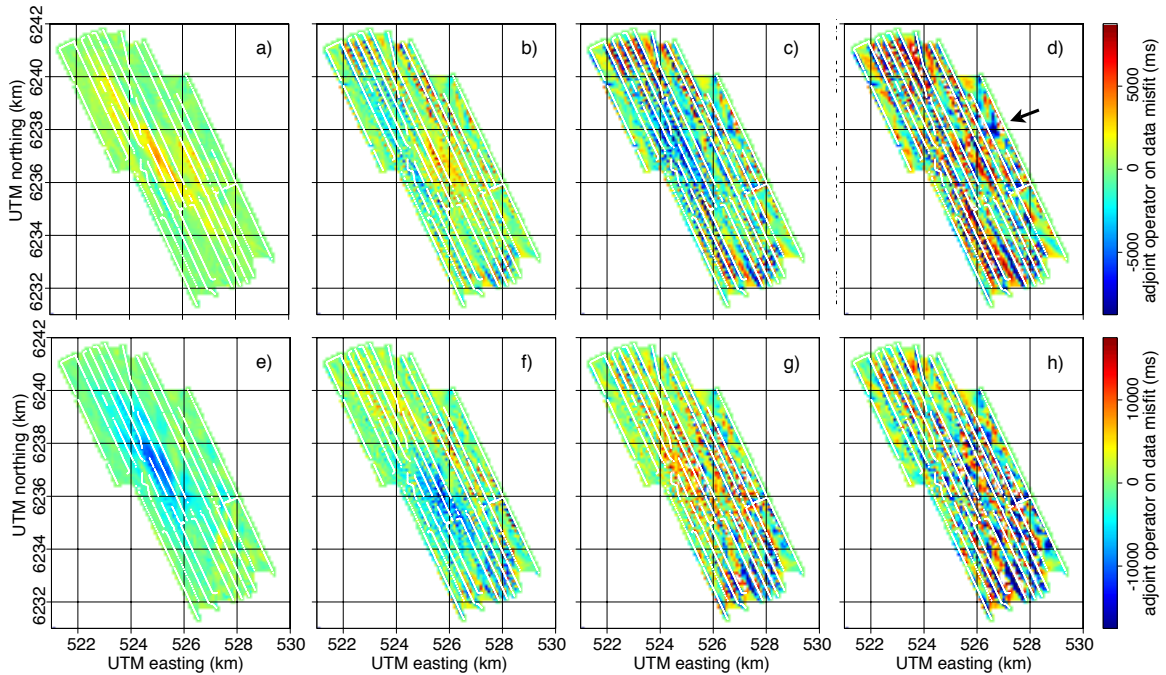


Figure 4.9: Adjoint of the tomographic operator applied to final data misfits in the Scholte-wave group-velocity tomographies for the stack of all crosscorrelations of 2010 data for central frequency range 0.75 – 0.95 Hz (top row) and 1.35 – 1.55 Hz (bottom row). Regularization: in a) and e)  $\epsilon = 0$ , in b) and f)  $\epsilon = 2.4 \times 10^7$ , in c) and g)  $\epsilon = 5.4 \times 10^7$ , in d) and h)  $\epsilon = 11.4 \times 10^7$ . The arrow indicates suppressed energy that ought to have been in the inverted model. [CR] joseph-all-vs-mres-eps-C3-C6

correlation fluctuation level (Chapter 3). Multiple independent stacks of crosscorrelations from a continuous sub-portion of a recording can be processed into independent velocity images.

In this section I present group-velocity images for 0.75–0.95 Hz and 1.35–1.55 Hz inverted from three vintages of data collected in 2004, 2005 and 2010. Tomographies are performed using EGFs retrieved by stacking the crosscorrelations for 6, 12, 24, 60 or 120 hours. The traveltimes pick procedure described earlier should make traveltimes picking insensitive to changes in the spectrum of the ambient seismic noise. The traveltimes selection criteria aims to normalize the inversion, such that the regularization strength ( $\epsilon$ ) is quantitatively approximately equal between inversions of two independent stacks. The problem is sufficiently over determined when selecting a large number of traveltimes picks. Even though the noise covariance of the traveltimes picks varies from inversion to inversion, the inverted models differ only a little. The effect of epsilon on the RMS difference between inverted perturbations is computed to determine whether the effects of the regularization parameter are quantitatively equal for inversions of independent stacks.

### **Scholte wave velocity images for 2004, 2005 and 2010**

Traveltimes are picked in vertical-to-vertical component EGFs of 6-, 12-, 24-, 60- and 120-hour stacks, and they are inverted for Scholte wave group-velocity images. The following three datasets are used: 24 hours of recording from 2004, 6 hours of recording from 2005, and a little over 5 days of recording from 2010. Scholte wave images based on 6-hour stacks can be computed for 2004, 2005 and 2010, based on 6-,12- and 24-hour stacks for 2004 and 2010, and based on 60- and 120-hour stacks for 2010. Only stations that were live during all recordings were selected.

Traveltimes picks with an SNR below 1.25, and for a minimum offset below 1500 m and a maximum offset above 6000 m are discarded. The maximum permitted anti-symmetry in traveltimes varied depending on the amount of recording time used when stacking crosscorrelations, and it generally decreases with increased stacked

Central frequency range (Hz)	6 hrs	12 hrs	24 hrs	60 hrs	120 hrs
0.75 – 0.95 Hz	0.0003	0.0002	0.000175	0.000125	0.0001
1.35 – 1.55 Hz	0.0008	0.0007	0.0005	0.0003	0.00025

Table 4.3: Traveltime pick acceptance criteria on the slowness equivalence of the anti-symmetry of the traveltime picks for causal and anticausal parts of the EGFs ( $\left\{ \frac{|t^+ - t^-|}{\Delta x} \right\}_{\max}$ ).

recording time. For traveltime picks between 0.75 – 0.95 Hz and between 1.35 – 1.55 Hz, the maximum anti-symmetry allowed is summarized in Table 4.3. These criteria were established by confirming that each inversion of group velocity images for 0.75–0.95 Hz and for 1.35–1.55 Hz had at least 900,000 and 1,000,000 traveltime picks available, respectively. Only the best 900,000 and 1,000,000 picks (based on SNR) were selected for inversions of group velocity images for 0.75 – 0.95 Hz and 1.35 – 1.55 Hz, respectively.

Using all data recorded in 2004 and for each central frequency range, six images can be computed on a 6-hour basis, two on a 12-hour basis, and one on a 24-hour basis. Example images and the mean and standard deviation of all images for the central frequency ranges 0.75 – 0.95 Hz and 1.35 – 1.55 Hz are shown in Figures 4.10 and 4.11 respectively. Using all data recorded in 2005, one image on a 6-hour stack basis can be computed for both frequency ranges (Figure 4.12). Using all data recorded in 2010 and for each central frequency range, twenty images can be computed on a 6-hour basis, ten on a 12-hour basis, and five on a 24-hour basis. Example images and the mean and standard deviation of all images for central frequency ranges 0.75 – 0.95 Hz and 1.35 – 1.55 Hz are shown in Figures 4.13 and 4.14, respectively. All images for both central frequency ranges computed from 2004, 2005 and 2010 data are included in Appendix D.

All Scholte-wave images presented in Figures 4.10 through 4.14 show the same features as imaged by the Scholte wave group-velocity images using the full stack of 2010 data (Figure 4.5). However, images derived from independent portions of the

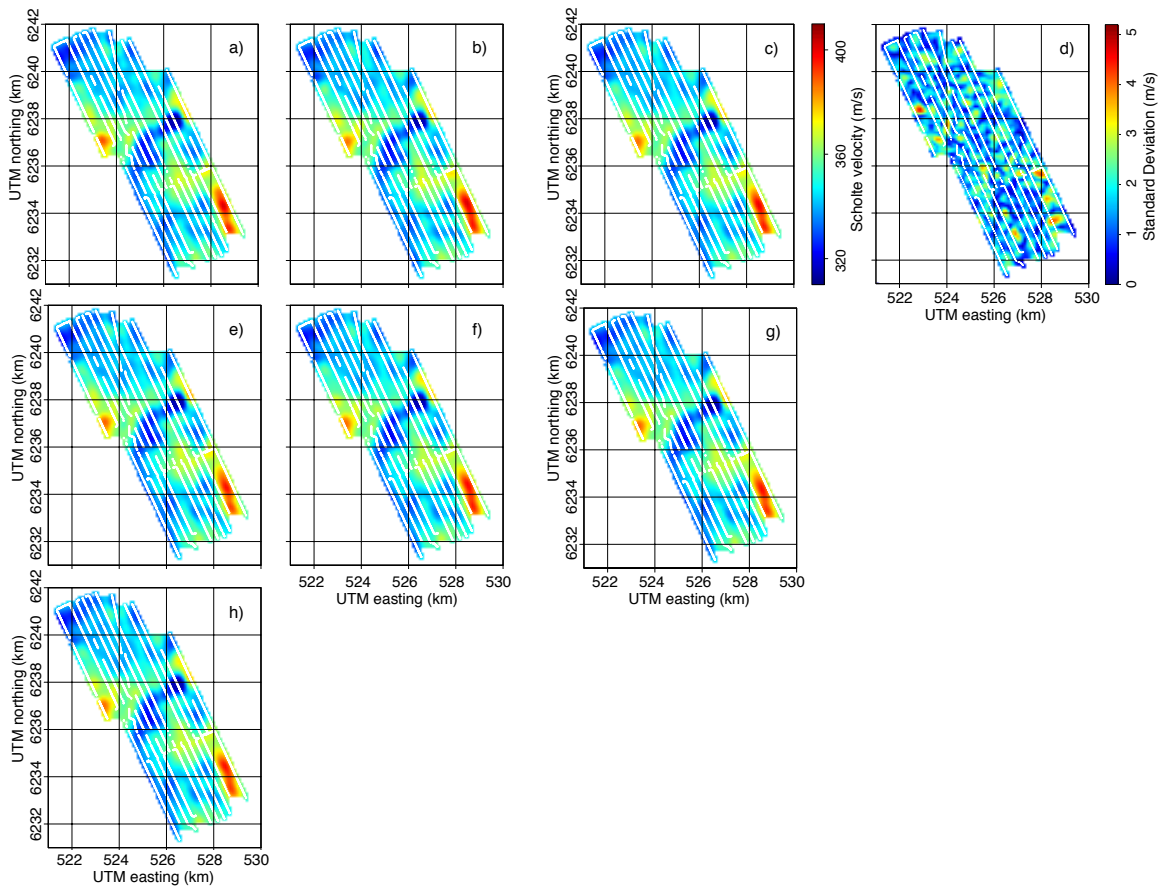


Figure 4.10: Scholte-wave group-velocity images for 0.75 – 0.95 Hz from non-overlapping consecutive stacks of crosscorrelations of 2004 data. Based on 6-hour stacks, two example images (a and b), the mean of all four images (c) and the standard deviation of all four images (d) are shown. Based on 12-hour stacks, two images (e and f) and their mean (g) are shown. Based on 24-hour stacks, one map (h) is shown. [CR] artman-tomo-C3

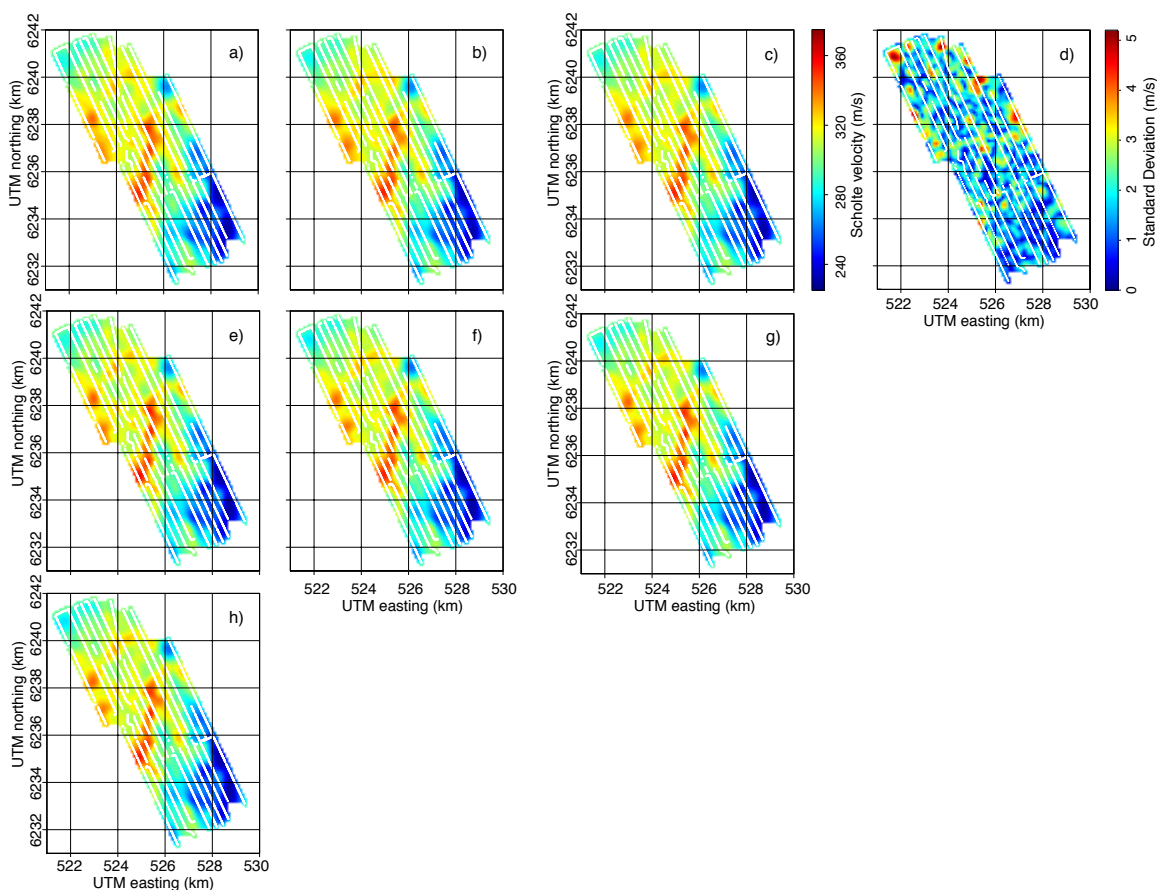
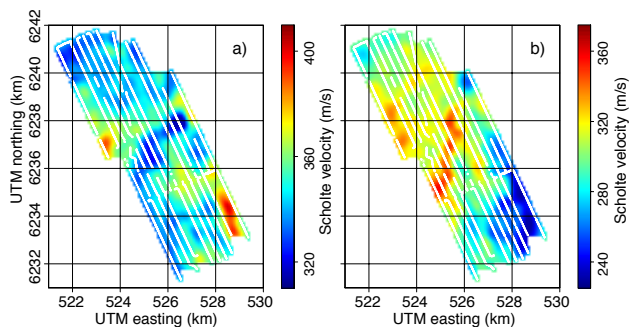


Figure 4.11: Scholte-wave group-velocity images for 1.35 – 1.55 Hz from non-overlapping consecutive stacks of crosscorrelations of 2004 data. Based on 6-hour stacks, two example images (a and b), the mean of all four images (c) and the standard deviation of all four images (d) are shown. Based on 12-hour stacks, two images (e and f) and their mean (g) are shown. Based on 24-hour stacks, one map (h) is shown. [CR] artman-tomo-C6

Figure 4.12: Scholte-wave group-velocity images for 0.75 – 0.95 Hz (a) and 1.35 – 1.55 Hz (b) from a consecutive 6-hour stack of crosscorrelations of 2005 data. [CR] jianhua-tomo-C3-C6



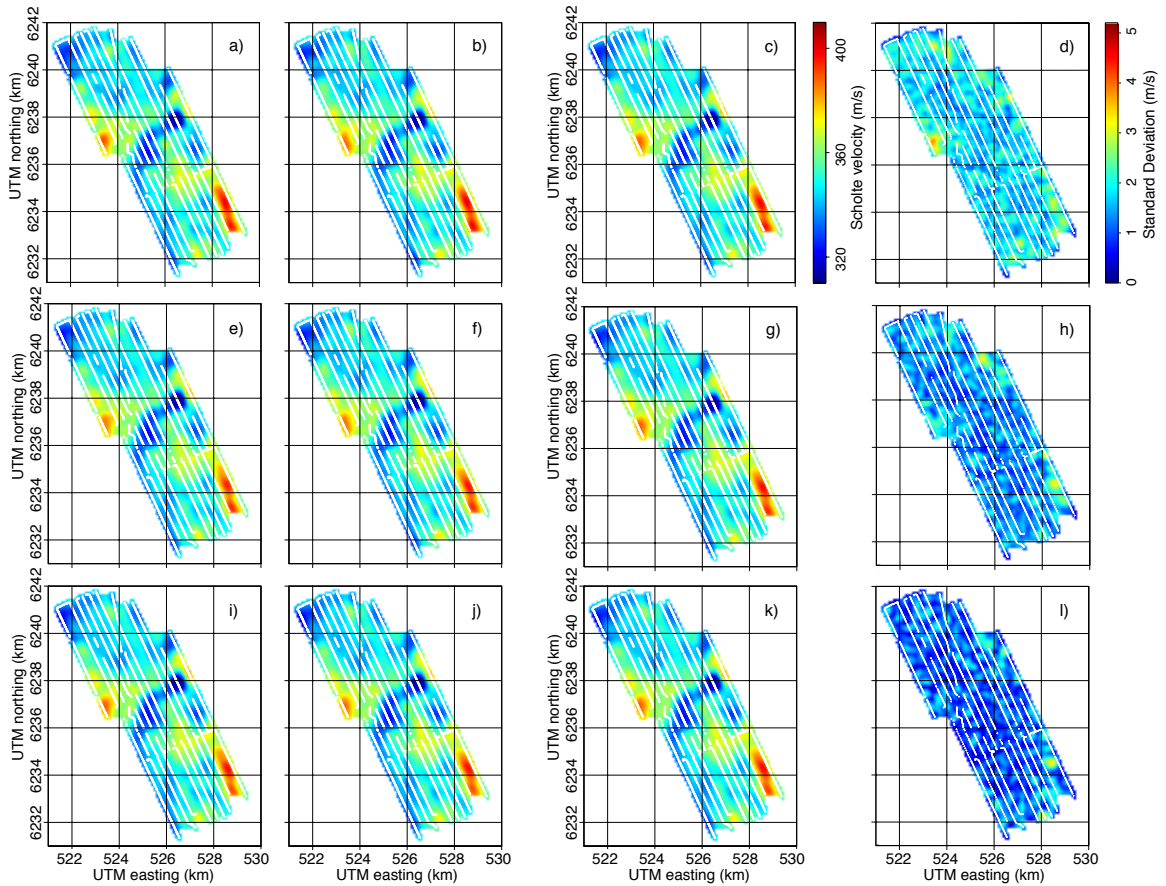


Figure 4.13: Scholte-wave group-velocity images for 0.75 – 0.95 Hz from non-overlapping consecutive stacks of crosscorrelations of 2010 data. Based on 6-hour stacks, two example-images (a and b), the mean all twenty images (c) and standard deviation all twenty images (d) are shown. Based on 12-hour stacks, two example images (e and f), the mean of all ten images (g) and standard deviation of all ten images (h) are shown. Based on 24-hour stacks, two example images (i and j), the mean all five images (k) and standard deviation all five images (l) are shown. [CR]

joseph-tomo-C3

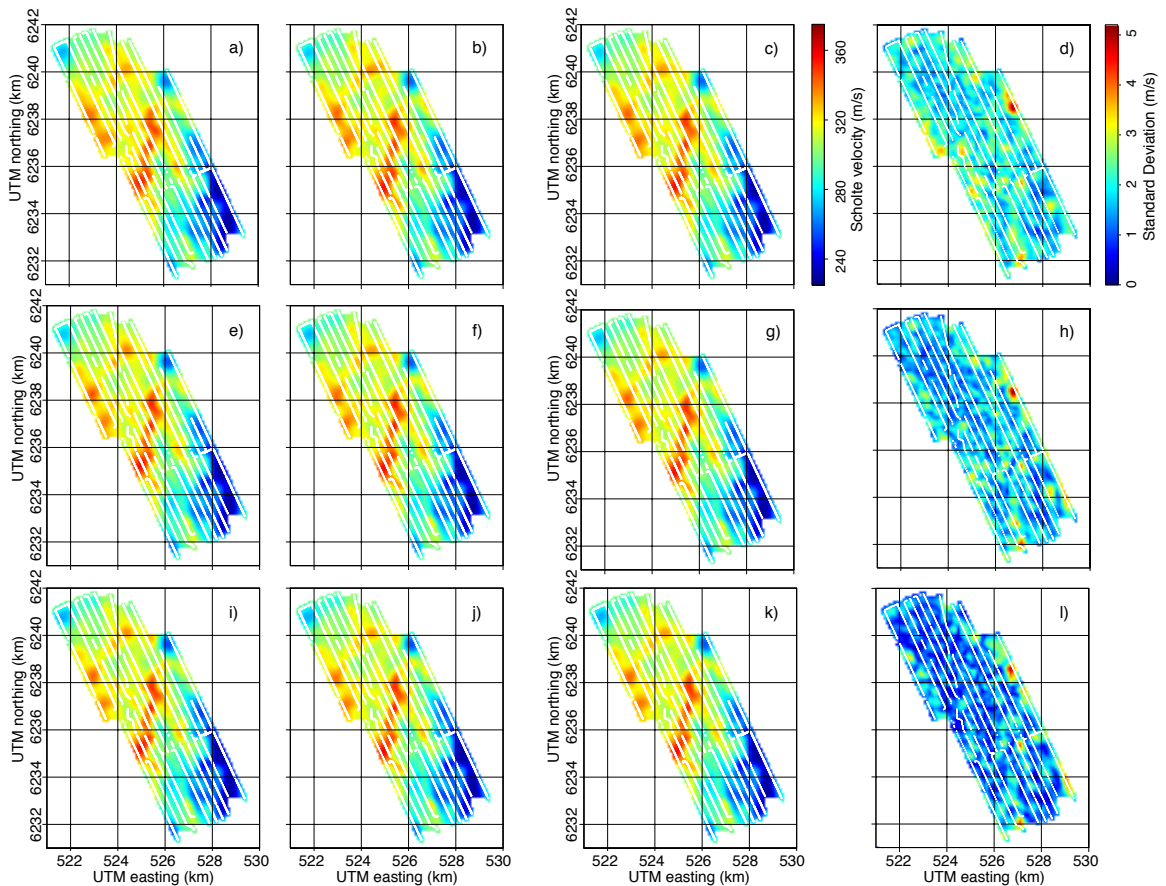


Figure 4.14: Scholte-wave group-velocity images for 1.35 – 1.55 Hz from non-overlapping consecutive stacks of crosscorrelations of 2010 data. Based on 6-hour stacks, two example-images (a and b), the mean all twenty images (c) and standard deviation all twenty images (d) are shown. Based on 12-hour stacks, two example images (e and f), the mean of all ten images (g) and standard deviation of all ten images (h) are shown. Based on 24-hour stacks, two example images (i and j), the mean all five images (k) and standard deviation all five images (l) are shown. [CR]

joseph-tomo-C6

recordings vary slightly. The standard deviation is largest for maps for the higher central frequency ranges from shorter stacks (Figure 4.14d), and the smallest standard deviation is for the lower central frequency range from longer stacks (Figure 4.13d). This variation will be further quantified in the next section.

## Temporal stability and temporal resolution of Scholte-wave group-velocity images

The tomographic inversion for velocity images is solved using a straight-ray sensitivity kernel with regularization by a Laplacian operator. The data fitting objective,  $\mathbf{F}\Delta\mathbf{m} = \Delta\mathbf{t}$ , and the model fitting objective,  $\nabla^2\Delta\mathbf{m} = \mathbf{0}$ , are balanced by the regularization strength,  $\epsilon$ . If  $\epsilon \rightarrow \infty$  then  $\Delta\mathbf{m} = \mathbf{0}$  is a solution and the velocity map will look the same. If  $\epsilon$  is relaxed, the inverted velocity images will contain features that predict the data, and the velocity images will look less alike because the data contain noise.

A difficulty in comparing two Scholte wave group-velocity images is the variable quantitative impact of a particular value of  $\epsilon$  per inversion. The regularization strength  $\epsilon$  weights the data-fitting and model-fitting objective functions based on an estimate of the noise covariance matrix in the data-fitting objective. The procedure to select traveltimes inverted for Figures 4.10 to 4.14 was meant to make  $\epsilon$  insensitive for a given quality of data and a given central frequency range. The quantitative impact of a particular value of  $\epsilon$  still varies between inversions of traveltimes from a 6-hour or 12-hour stack, but it is approximately the same for inversions of traveltimes from equally long stacks. To test whether  $\epsilon$  is normalized in this fashion, the average variation between inverted slowness perturbation images is compared as a function of epsilon. One measure for such variation is the RMS difference between two inverted perturbation maps, averaged over the cells covered by the tomography. This RMS difference can then be averaged for all possible combinations of perturbation maps (in the set  $\Delta\bar{\mathbf{m}}(\mathbf{x}) = (\Delta\mathbf{m}_1(\mathbf{x}), \Delta\mathbf{m}_2(\mathbf{x}), \dots, \Delta\mathbf{m}_M(\mathbf{x}))$ ) within a given set

of velocity perturbations:

$$\text{RMS}_1 = \frac{2}{M(M-1)} \sum_{i=1}^M \sum_{j=1}^i \sqrt{\frac{1}{T} \sum_{\mathbf{x}} [\Delta \mathbf{m}_i(\mathbf{x}) - \Delta \mathbf{m}_j(\mathbf{x})]^2 \mathbf{C}(\mathbf{x})}, \quad (4.5)$$

where  $T$  is the cardinality of the set in the masking matrix,  $\mathbf{C}(\mathbf{x})$ , selecting the area covered by the LoFS array:  $T = |\{\mathbf{C}(\mathbf{x}) \neq 0\}|$ .  $M$  is the number of perturbation maps in the subset (for 2010 data  $M = 20$  for maps from 6-hour stacks,  $M = 10$  for maps from 12-hour stacks,  $M = 5$  for maps from 24-hour stacks).

Figure 4.15 shows the curves of averaged RMS difference of inverted velocity perturbations versus regularization strength. The color denotes the subset and the symbols denote the amount of stacked crosscorrelations. Figure 4.15a contains averaged RMS difference between maps for a central frequency range of 0.75 – 0.95 Hz. Figure 4.15b shows the averaged RMS difference between maps for a central frequency range of 1.35 – 1.55 Hz. The averaged RMS differences are lower when using traveltimes based on longer stacking time. The curves for 12-hour stacks and for 6-hour stacks from 2004 overlap those of 2010 (Figure 4.15a). This means that  $\epsilon$  is quantitatively approximately the same for all inversions on a 6-hour basis and on a 12-hour basis, but differs when comparing inversions on a 6-hour basis with inversions on a 12-hour basis.

There are several factors to consider when determining what regularization strength is appropriate (Aster et al., 2005). One consideration is the tradeoff between the data-fitting objective,  $\mathbf{F}\Delta\mathbf{m} = \Delta\mathbf{t}$ , and the model-fitting objective,  $\nabla^2\Delta\mathbf{m} = \mathbf{0}$ . Figures 4.16 and 4.17 show the trade off between model residual versus data residual as a function of regularization strengths for inversions for central frequency ranges 0.75 – 0.95 Hz and 1.35 – 1.55 Hz, respectively. The graphs in the right columns of figures 4.16 and 4.17 each show the magnitude of the model residual versus magnitude of the data residual as a function of regularization strength in color (Figures 4.16a to 4.16c and 4.17a to 4.17c for tomographies on a 24-hour, 12-hour and 6-hour basis, respectively). The graphs in the right column of Figures 4.16 and 4.17 each show the derivative of the magnitude of the model residual

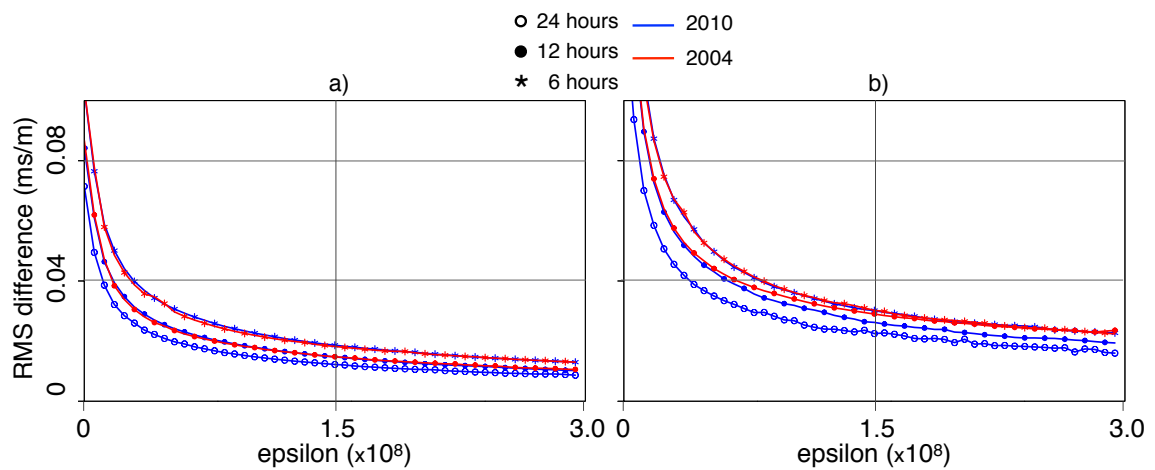


Figure 4.15: Average RMS differences between inverted Scholte-wave group-velocity perturbations, averaged over all combinations of tomography results, for 0.75 and 0.95 Hz (a) and 1.35 and 1.55 Hz (b). Colors and symbols denote subsets subsets of the tomography results: red denotes averaging between 2004 results, blue denotes averaging between 2010 results. Open circles denote averaging between tomography results on a 24-hour basis, filled circles denote averaging between tomography results on a 12-hour basis, asterisks denote averaging between tomography results on a 6-hour basis. [CR] RMS-vs-eps-1

versus magnitude of the data residual as a function of regularization strength (Figures 4.16 d to 4.16 f and 4.17 d to 4.17f for tomographies on a 24-hour, 12-hour and 6-hour basis, respectively). Both magnitudes are normalized with respect to their value when  $\epsilon = 0$ . The scatter points each denote a tomography problem that together form lines as a function of regularization strength (Figures 4.16a to 4.16c and Figures 4.17a to 4.17c).

Choosing a higher regularization strength to force a low variability between maps from independent stacks will negatively impact the amplitude and resolution of the inverted anomalies. For each inversion of the 2010 data, the averaged RMS differences are plotted against the magnitude of the model residual (Figures 4.18a and 4.18b for inversions for a central frequency range 0.75–0.95 Hz and 1.35–1.55 Hz, respectively). The averaged RMS differences are always larger for maps computed on shorter stacks of crosscorrelations.

Increasing the regularization strength initially suppresses effects of noise and acquisition imprint. But the effect of increasing the regularization strength on the magnitude of the model residual gradually diminishes while geologically relevant information in the data starts to be suppressed (Figure 4.4).

One way to quantify the temporal uncertainty in a particular velocity image is to present the standard deviation for the set of images. For data from 2010, velocity images  $v(\mathbf{x}) = \mathbf{m}^{-1}$  are inverted from the 6-hour, 12-hour and 24-hour stacks. This results in sets of estimates,  $\bar{\mathbf{v}}(\mathbf{x}) = (\mathbf{v}_1(\mathbf{x}), \mathbf{v}_2(\mathbf{x}), \dots, \mathbf{v}_M(\mathbf{x}))$ , where  $M$  is 20, 10 and 5 for the 6-hour, 12-hour and 24-hour sets of velocity images, respectively. The unbiased estimation of standard deviation,  $\sigma = \sigma(\mathbf{x})$ , for these sets were calculated according to the following equations by Walpole et al. (2011):

$$\sigma^2 = \frac{1}{M-1} \sum_{i=1}^M [v_i - \bar{v}]^2, \quad (4.6)$$

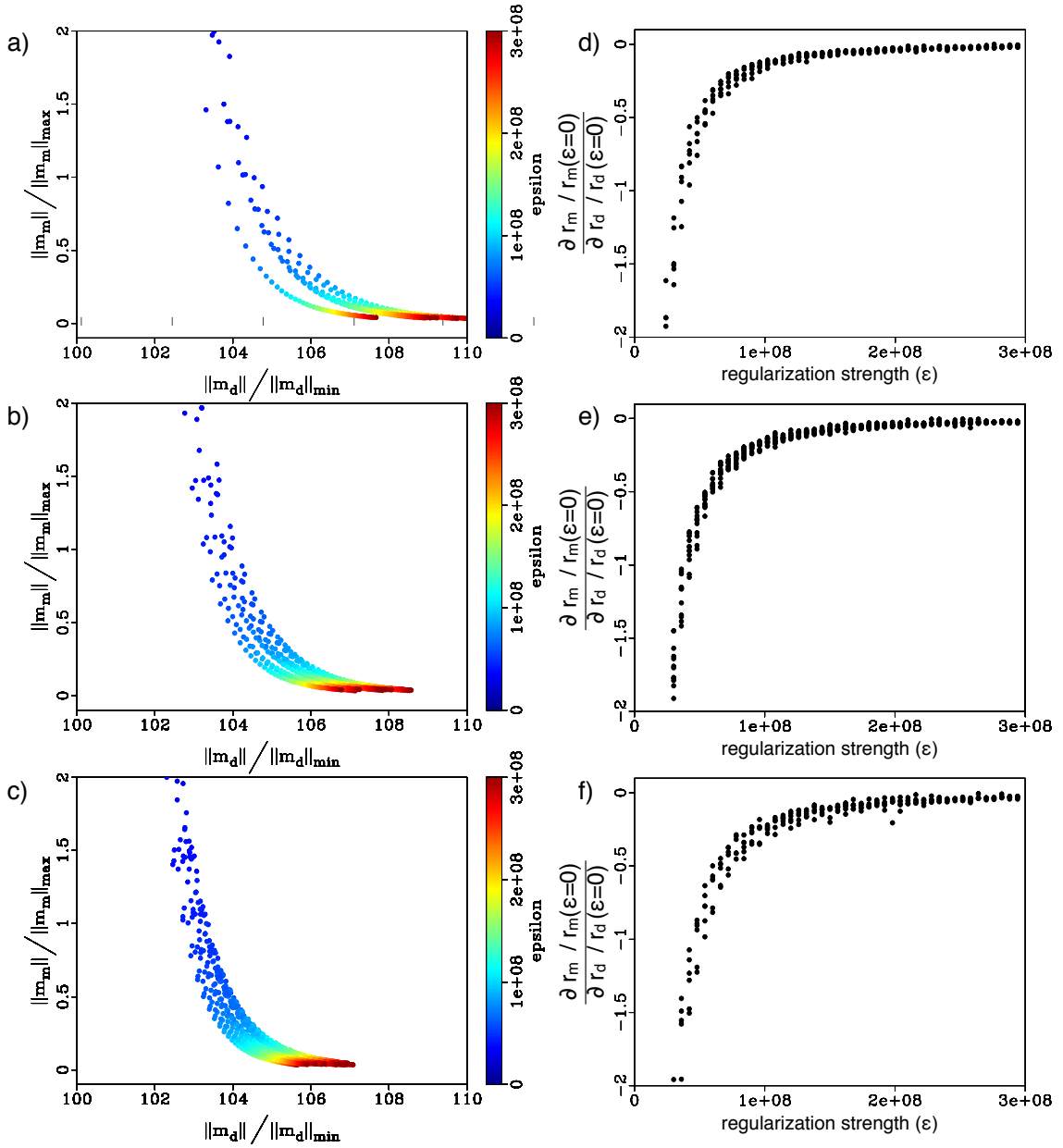


Figure 4.16: Scatterplot of normalized magnitude of the model residual versus normalized magnitude of the data residual for solutions of all the tomographic inversions of Scholte-wave group-velocity images for 0.75 – 0.95 Hz. The coloring denotes regularization strength ( $\epsilon$ ) in the inversions: for 24-hour stacks in (a), 12-hour stacks in (b) and 6-hour stacks in (c). Derivatives of the normalized magnitude of the model residual with the normalized magnitude of the data residual for the data in a) to c) plotted versus regularization strength in respectively d) to f). [CR] rd-vs-rm-C3

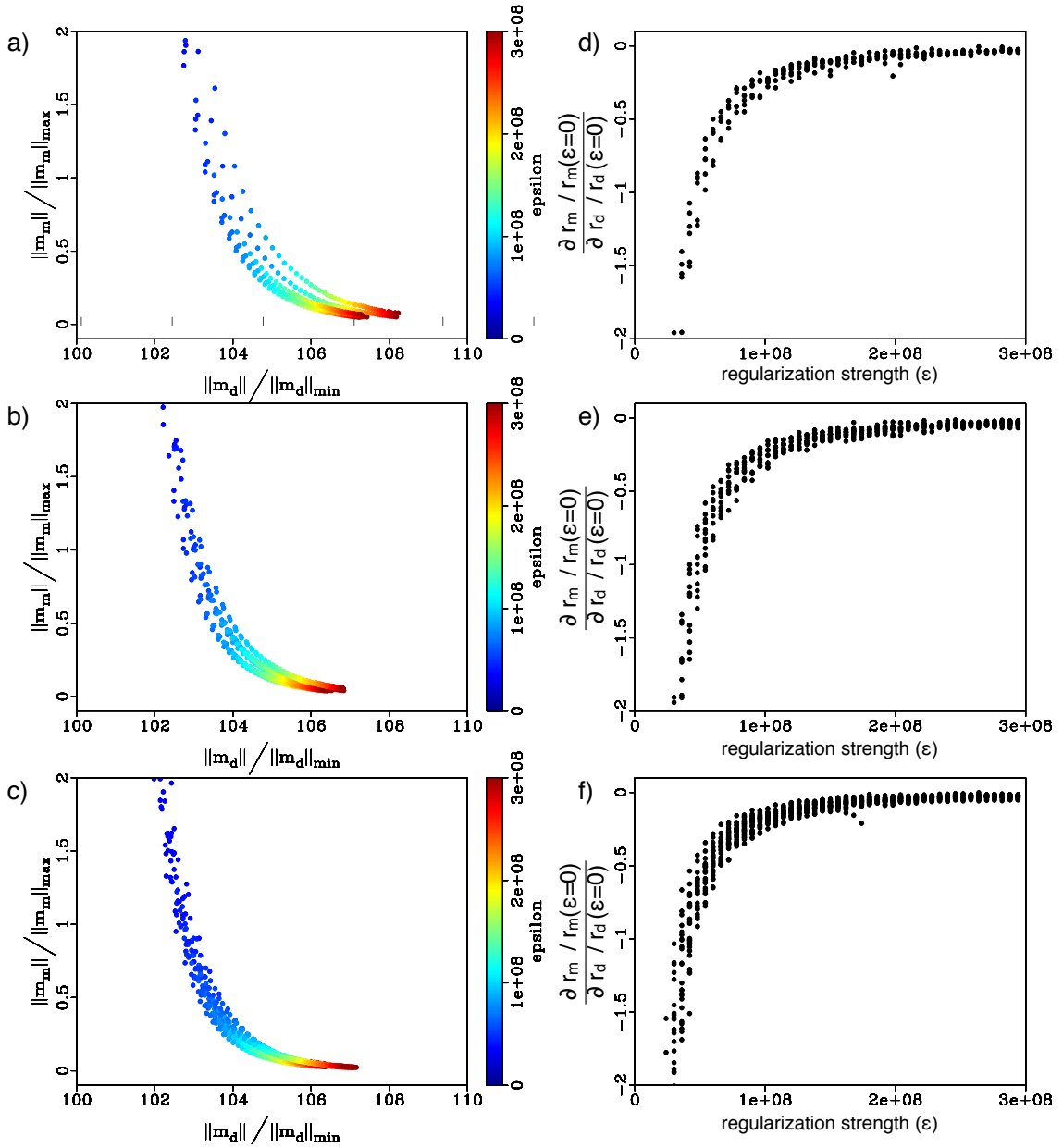


Figure 4.17: Scatterplot of normalized magnitude of the model residual versus normalized magnitude of the data residual for solutions of all the tomographic inversions of Scholte-wave group-velocity images for 1.35 – 1.55 Hz. The coloring denotes regularization strength ( $\epsilon$ ) in the inversions: for 24-hour stacks in (a), 12-hour in (b) and 6-hour stacks in (c). Derivatives of the normalized magnitude of the model residual with the normalized magnitude of the data residual for the data in a) to c) plotted versus regularization strength in respectively d) to f). [CR] rd-vs-rm-C6

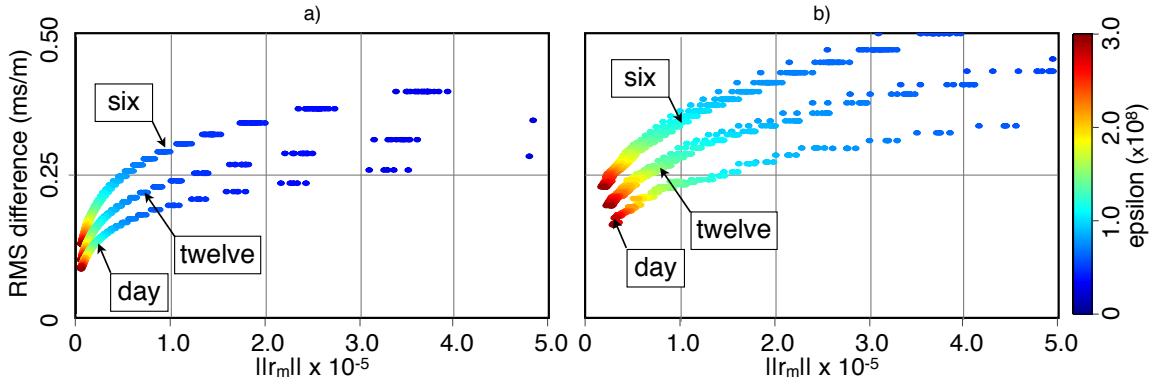


Figure 4.18: Scatterplot showing the relationship between averaged RMS difference versus the magnitude of the model residual with the regularization strength in color.

[CR] RMS-vs-rm

where  $\bar{v} = \bar{v}(\mathbf{x})$  denotes the arithmetic mean of velocities and is computed as

$$\bar{v} = \frac{1}{M} \sum_{i=1}^M v_i. \quad (4.7)$$

## DISCUSSION

The dispersive nature of surface waves is the basis for imaging velocity structures at depth using surface wave tomography. Longer wavelengths at lower frequencies provide sensitivity away from the interface of propagation (Aki and Richards, 2002). Group velocities of interface waves can be found for packages of energy isolated within a narrow frequency range (Claerbout, 1976). Traveltimes for group velocities are effectively isolated for a central frequency range by a narrow bandpass of the crosscorrelation gathers (Figure 4.2b and c).

The tomography problem is solved by a conjugate direction scheme of the least squares solution and is regularized by a second order Tikhonov regularization (penalizing spatial second derivatives). The choice of the regularization strength is subjective. The regularization strength should typically be related to the frequency-dependent

wavelength and should regularize the null-space of the inversion. An optimum regularization strength can usually be found through an L curve analysis (Aster et al., 2005). However, the station coverage throughout the model space and dense ray-paths change the nature of the tomographic inversion such that an L-curve analysis does not readily provide an optimum regularization strength. Scanning the inverted group velocity images versus regularization strength (epsilon) (Figure 4.4) shows that a small increase of epsilon cleans the images of the most geologically-unreasonable features (compare Figure 4.4b with 4.4a and Figure 4.4l with 4.4k). But streaks remain in the velocity images in between the cables. These streaks thus are an acquisition imprint. The regularization strength must increase considerably before those acquisition imprints start to disappear.

The velocity contrasts we are imaging are low relative to the footprint artifacts. Analysis of curves showing the trade-off between model- and data-fitting objectives do not show a clear optimum epsilon over the range where the regularization strength suppresses acquisition footprint artifacts. The vertical axis in figures 4.16 and 4.17 can be scaled to create an apparent corner at higher or lower regularization strengths, so the L curve analysis is ambiguous. I selected a regularization strength that lies a little higher than where the L curve analysis would suggest based on appearances and a reasonable suppression of acquisition footprint. Analyzing the suppressed energy in the model space (Figure 4.9) confirms that over the range of epsilon that suppress the acquisition footprint almost no energy is suppressed that belongs in the model space. The only exception is some energy related to the very high velocity contrast at the border between low-velocity anomaly A and high-velocity anomaly C (Figure 4.7) that appears in the data residual at the selected regularization strength (Figure 4.9d).

Several subsurface features are imaged with group-velocity tomography for a set of central frequency ranges (Figure 4.5). The wavelengths for fundamental-wave Scholte waves ranges from over 550 m for the lowest central frequency range to 390 m (Chapter 3). The Scholte wave group-velocity images have an integrated sensitivity over depth (Aki and Richards, 2002) with a peak sensitivity at approximately half the wavelength. Thus the Scholte waves are expected to be able to image about 275 m

under the sea floor. The three-dimensional P-wave velocity structure at Valhall is independently known from regular controlled-source seismic surveying (Sirgue et al., 2010). Four depth slices through a cube of P-wave velocities are shown in Figures 4.19a to d, at 217.5 m, 172.5 m, 127.5 m and 82.5 m below the sea floor, respectively. Controlled-source images extend over an area much larger than the LoFS array, thus the images in Figure 4.19 extend beyond the area covered by the receiver array. The images obtained from ambient-seismic-noise tomography are confined within the area of the recording array. Although P-wave velocity and Scholte group velocities are different physical parameters, their spatial distribution is likely to be related.

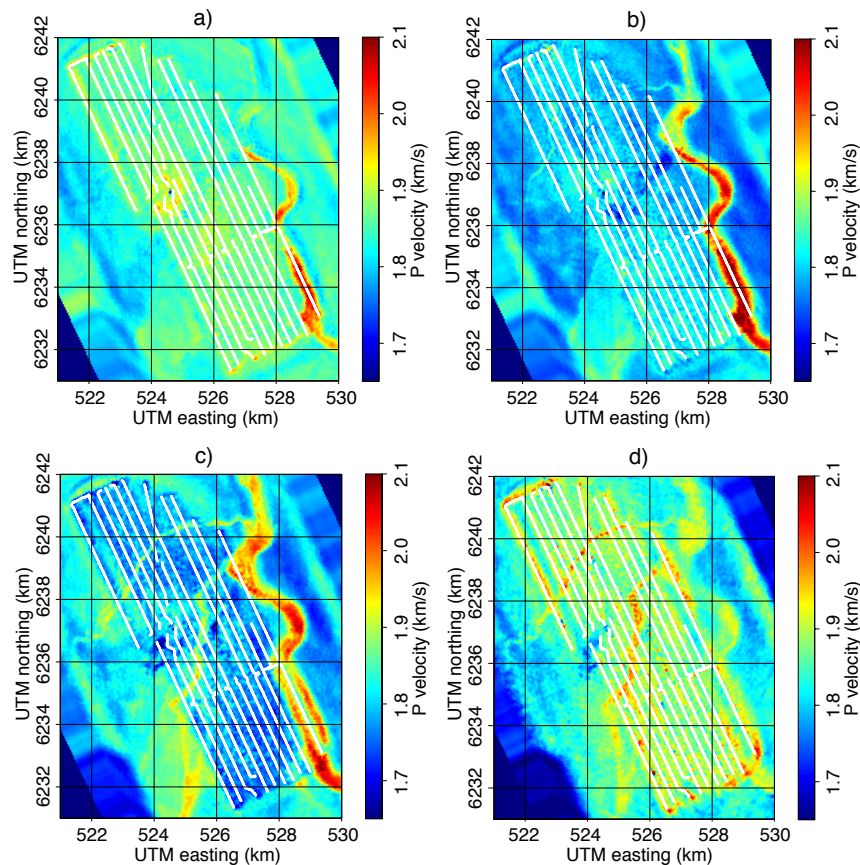


Figure 4.19: Image of P-wave velocities obtained using waveform inversion of controlled-source P-wave data (Sirgue et al., 2010), courtesy BP. Velocity slices 217.5 m (a), 172.5 m (b), 127.5 m (c) and 82.5 m (d) below the sea floor. [NR]

fwi4

The low-velocity anomaly (A in Figure 4.7) that crosses the center of the array from southwest to northeast, from UTM (525, 6235.5) km to UTM (526.5, 6238) km, just south of the main platform corresponds to a series of anomalies in Figure 4.19b. There is a paleochannel, 100 to 250 meters deep, that meanders into the southeastern corner of the array and touches the array along the eastern edge near UTM (526.5, 6239) km. This channel is clearly imaged in all but the highest central frequency ranges (B and C in Figure 4.7). At the higher central frequencies (1.15 – 1.55 Hz), meandering channels cross the array south to north (approximately from UTM (525, 6235) km to UTM (526, 6238.5) km) and a less well defined channel that crosses the northern end of the array east to west (from UTM (523, 6238.5) km to UTM (525, 6240) km) (D and E in Figure 4.7). These correspond to paleochannels at shallower depths in the subsurface (Figures 4.19c and d). In the higher central frequencies (1.15 – 1.55 Hz), a large oval-shaped background higher velocity zone found over the northern part of the array was identified in Scholte-wave velocity images from controlled-source seismic surveying (Hatchell et al., 2009). Wills et al. (2008) interpreted these to represent contractional and extensional strains caused by production-related seafloor subsidence at Valhall.

The Love-wave group velocity images in Figure 4.6 do not directly correspond to known subsurface paleochannels. There are no published maps of Love-wave velocities, because they are poorly excited by controlled sources at the sea surface. One profile of Love waves group velocities between 3 and 29 Hz was extracted on radial lines away from the platform using the platform as a noise source (Mordret et al., 2013a). The frequency content of their profile does not overlap with the frequency content in the microseism energy imaged in this chapter. However, their group-velocities above 3 Hz are approximately 300m/s (and decrease with increasing frequencies). This is consistent with the average group velocities of approximately 315 m/s at 1.5 Hz (Table 4.2). The longer wavelengths of Love waves makes them sensitive to features at deeper depths than the feature imaged by Scholte waves at the same frequencies. The most dominant feature is the large oval-shaped zone of higher background velocity with the same dimensions as found in the highest central frequency ranges of the Scholte waves. Considering that Love-wave particle motion

occurs in the horizontal plane, it is conceivable that the contractional and extensional strains caused by production-related seafloor subsidence at Valhall dominate the Love-wave propagation more than the Scholte-wave propagation.

The ray coverage is generally excellent throughout the array. A checkerboard test indicates that, except for the northern edge of the array and the area under the platform, anomalies can be constrained in all directions. The spatial resolution of the tomography is not determined by ray coverage (which is generally very high). Rather, the resolution is constrained by the straight-ray approximation and noise covariance in the data. The noise covariance is difficult to estimate, but the traveltimes picking procedure was designed to keep traveltimes sets with approximately the same ensemble-quality for stacks of the same size. Although the uncertainty of one pick cannot be easily quantified, the inconsistency of picks in nearby adjacent traces shows the effect of noise. Assuming the noise is normally distributed and independent from trace to trace, the use of regularization removes the effect of noise from the least-squares solution. Because the inversion problem is over-determined (about a million data points to constrain about five thousand model parameters).

By analyzing the results obtained with variable length stacks, the variability between inverted Scholte-wave images due to the residual background correlation fluctuations can be estimated. Tomographies of partial stacks of 2010 data provide 20 images based on a 6-hour stack, 10 images based on a 12-hour stack and 20 images based on a 24-hour stack. The main difficulties with comparing one map to another are the quantitatively varying value of regularization strength and variation in the spectrum of the ambient noise. However, after spectral balancing before picking, and using a constant number of traveltimes picks, the regularization strength for a given value of  $\epsilon$  is approximately the same from one inversion to the next. This is determined by judging the RMS difference between inverted slowness perturbation maps using stacks of smaller portions of data. The average RMS difference between inverted perturbations from 6-hour stacks using 2004 data overlies the average RMS difference from 6-hour stacks using 2010 data (for central frequency range 0.75 – 0.95 Hz). This

also applies to the average RMS difference based on 12-hour stacks (for central frequency ranges 0.75 – 0.95 Hz and 1.35 – 1.55 Hz). An exception is the average RMS difference as a function of regularization strength for 12-hour stacks for 1.35 – 1.55 Hz. In this case the crosscorrelation stack may not yet have converged and the EGFs are not sufficiently stable, so the noise is not normally distributed and independent from one pick to another. However, for the 6-hour stack the RMS curves for 2004 and 2010 overlay for 1.35 – 1.55 Hz. Because only two images were available for 12-hour stacks from 2004, the difference between the two may not be an accurate representation of the expected RMS difference on a 12-hour basis. The good match between the average RMS differences for 2004 and 2010 as a function of regularization strength demonstrates that the picking procedure effectively enables a direct comparison of 2004, 2005 and 2010 data. Despite that the 2004 and 2005 data were recorded with a standard-acquisition low-cut filter which was not applied when recording the 2010 data (Chapter 2).

Spatial maps of the standard deviation between inverted velocity images generally show very small variance between images. As expected the standard deviation is largest for images for the higher central frequency ranges from shorter stacks and smallest for the lower central frequency range from longer stacks. There are small areas with more variation where anomalies in those areas should not be over interpreted.

## CONCLUSIONS

Crosscorrelations of microseism noise recorded by Valhall's LoFS array are inverted into credible velocity models imaging the top 250 m. The Scholte-wave velocity correlates well with the subsurface lithology known from full-waveform inversion of controlled-source P-wave seismic data. The Love wave group-velocity images are dominated by smoother shapes that may relate to the production-altered stress-state of the reservoir's overburden. Love and Scholte waves thus provide complementary

information on the subsurface. Tomography using the vertical-to-vertical component crosscorrelations yields Scholte-wave velocity maps with high repeatability. The traveltimes picking procedures are insensitive to the transient spectrum of the ambient seismic noise. So the inverse problem can be posed in a way that normalizes the regularization strength for a particular crosscorrelation stack-length. Thus images derived from different recordings can be directly compared for a given regularization strength. The variation between velocity images decreases with lower frequency and longer stack lengths.

## ACKNOWLEDGMENTS

My thanks to BP and the partners of the Valhall Field (BP Norge and Hess Norge) for permission to publish the data in this chapter. My thanks to Olav Barkved, Joe Dellinger, Damien Dieulangard, John Etgen, Einar Kjos and Jianhua Yu of BP for helpful discussions and suggestions and for access to the data. I thank Matthew Haney for his suggestions in the review for a paper (de Ridder and Biondi, 2013) that spurred the RMS analysis in this and the next chapters. I thank Bob Clapp for many comments and suggestions that substantially improved this chapter.